Dalton Transactions

ROYAL SOCIETY OF CHEMISTRY

PAPER

View Article Online
View Journal | View Issue

Check for updates

Cite this: *Dalton Trans.*, 2024, **53**, 17620

Utilisation of *in situ* formed cyano-bridged coordination polymers as precursors of supported Ir–Ni alloy nanoparticles with precisely controlled compositions and sizes†

Yusuke Yamada, *[a,b] Miho Nishida,[a] Tatsuya Nakabayashi,[a] Takashi Nakazono,[b] Hanghao Lin,[a] Pengru Chen [a] and Masazumi Tamura *[a,b]

Received 22nd August 2024,
Accepted 30th September 2024

DOI: 10.1039/d4dt02386b

rsc.li/dalton

Ir–Ni alloys supported on SiO_2 have been reported to show high catalytic activity for styrene hydrogenation; however, precise control of compositions and sizes of the Ir–Ni alloys is difficult when conventional metal salts are used as precursors. Furthermore, the concomitant formation of unalloyed Ni nanoparticles disturbs quantitative discussion about Ir–Ni alloy compositions. We report herein a preparation method of Ir–Ni alloys with precisely controlled compositions on SiO_2 using $Ni(NO_3)_2$ and an Ir complex possessing CN^- ligands, $[Ir(CN)_6]^{3-}$ or $[Ir(ppy)_2(CN)_2]^-$ (ppy = 2-phenylpyridine), as precursors. The *in situ* formation of cyano-bridged coordination polymers involving Ir and Ni promotes the formation of Ir–Ni alloys, whose compositions are virtually the same as expected from the amounts of Ir and Ni used for the preparation, after heat treatment under H_2. The use of $[Ir(ppy)_2(CN)_2]^-$ as the precursor resulted in the formation of smaller Ir–Ni alloy particles than those with $[Ir(CN)_6]^{3-}$ related to the structures of the formed coordination polymers.

Introduction

Hydrogenation of olefins and aromatic compounds catalysed by supported metal catalysts is widely used in industrial processes for petro-, coal-, and fine-chemicals.[1–9] For example, supported Pt- or Pd-based catalysts are most frequently used,[10–12] and Rh- and Ir-based catalysts have also emerged as a new class of catalyst.[13–17] The catalytic behaviour of metal catalysts can be modified by forming alloys with a foreign metal.[18–23] Classically, the forms of alloys can be categorized into two groups: one is solid solutions in which two metals are completely disordered in a solid; and the second is intermetallic alloys in which two different metals are periodically aligned similarly to molecules. Recently, more sophisticated structures such as core–shell have been adopted for rational catalysis enhancement.[24–27] The catalytic activity and selectivity of single-atom alloys attract much attention because of their high potential with precise control of electronic and geometric structures around the single atom.[7,28–40]

Single-atom alloys of Ni and Ir metals as guest and host metals, respectively (Ir–Ni alloy), loaded on SiO_2 have been reported to exhibit high catalytic activity for styrene hydrogenation selective for ethylbenzene.[41] The styrene hydrogenation is industrially important because styrene formed during gasoline pyrolysis provides troublesome gums, resulting in the choking of pipelines.[42,43] The Ir–Ni alloy catalysts have been prepared by the sequential impregnation method using H_2IrCl_6 and $Ni(NO_3)_2$ as precursors in previous reports.[41] The prepared Ir–Ni alloys supported on SiO_2 exhibited catalytic activity for styrene hydrogenation that was significantly higher than that for unalloyed monometallic catalysts.[41] A proposed reason for the high catalytic activity is the formation of half-hydrogenated styrene adsorbed on both a Ni single atom and

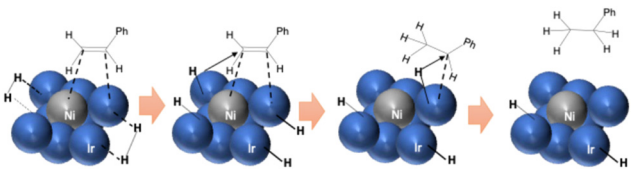

Scheme 1 The proposed catalytic mechanism for styrene hydrogenation on an Ir–Ni alloy.[44]

[a]*Department of Chemistry and Bioengineering, Graduate School of Engineering, Osaka Metropolitan University, Osaka 558-8585, Japan. E-mail: ymd@omu.ac.jp*
[b]*Center for Artificial Photosynthesis, Osaka Metropolitan University, Osaka 558-8585, Japan*

†Electronic supplementary information (ESI) available: Schematic drawing, IR, PXRD, EDX line scanning spectra, and the size distribution of Ir–Ni alloy particles observed by TEM. See DOI: https://doi.org/10.1039/d4dt02386b

an adjacent Ir atom surrounded by H species adsorbed on Ir metals (Scheme 1).[44] As a result, the activation energy for the hydrogenation of styrene decreased by about 20 kJ mol^{-1}.[44] The composition of the Ir–Ni alloy has been reported to influence the catalytic activity, although the unalloyed Ni metal concomitantly generated on the SiO_2 surfaces was catalytically inactive (Scheme S1†). The precise control of the Ir–Ni alloy composition is hardly possible when preparation methods with conventional precursors are used. *In situ* formation of multinuclear complexes containing both Ir and Ni by sequential impregnation could be a promising method to avoid the formation of unalloyed Ni metals.

Metal complexes with cyano ligands such as hexacyanometallates are known to coordinate with a foreign metal ion to form heterometallic multinuclear complexes.[45–52] The cyano ligand can be removed by thermal treatments below ~300 °C so that cyano-bridged complexes can be converted into metal oxides and/or alloys.[53] For example, Fe–Co alloy/carbon composites have been reported to be prepared by *in situ* pyrolysis of cyano-bridged Fe and Co complexes with precisely controlled Fe/Co ratios.[11] Therefore, cyano-bridged iridium and nickel complexes could be promising precursors for Ir–Ni alloys with precisely controlled compositions.

We report herein the preparation of Ir–Ni alloys supported on metal oxide supports (M_AO_B = SiO_2, SiO_2-Al_2O_3, TiO_2) by using $Ni(NO_3)_2$ and an Ir complex, *i.e.*, $[Ir(CN)_6]^{3-}$ with six cyano ligands or $[Ir(ppy)_2(CN)_2]^-$ (ppy = 2-phenylpyridine) with two cyano ligands, as precursors (Scheme 2). First, a series of Ir–Ni alloys supported on SiO_2 were prepared by using $[Ir(CN)_6]^{3-}$, which forms a three-dimensional reticular structure with Ni^{2+}. Next, Ir–Ni alloys supported on M_AO_B were furnished by using $[Ir(ppy)_2(CN)_2]^-$, which forms a one–dimensional linear structure with Ni^{2+}. Moreover, the catalytic activity of Ir–Ni alloys supported on M_AO_B was evaluated for styrene hydrogenation. This is the first report using cyano-bridged Ir–Ni complexes as precursors of Ir–Ni alloys with precisely controlled compositions supported on metal oxides.

Experimental section

Materials

All chemicals were obtained from chemical companies and used without further purification unless otherwise noted.

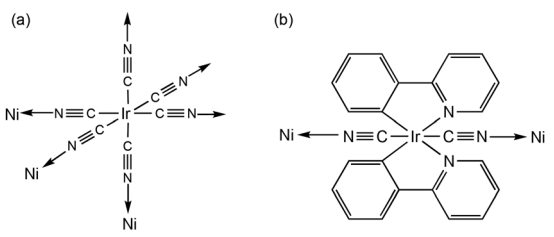

Scheme 2 Partial structures of *in situ* formed coordination polymers containing Ni and (a) $[Ir(CN)_6]^{3-}$ (**Ir(CN)$_6$**) or (b) $[Ir(ppy)_2(CN)_2]^-$ (**Ir(CN)$_2$**).

Potassium hexacyanoiridium(III) ($K_3[Ir(CN)_6]$) was obtained from Kishida Chemical Co., Ltd. Potassium cyanide (KCN), nickel(II) nitrate hexahydrate ($Ni(NO_3)_2$, 99.9%), acetonitrile (CH_3CN), ethanol (C_2H_5OH, 99.5%), toluene, and *n*-dodecane were obtained from FUJIFILM Wako Pure Chemical Corporation. Iridium(III) chloride hydrate ($IrCl_3{\cdot}xH_2O$), 2-phenyl pyridine (ppy) and tetra-*n*-butylammonium chloride (TBACl) were purchased from Tokyo Chemical Industry Co., Ltd. SiO_2 obtained from Fuji Silysia Chemical Ltd was calcined before use in air at 973 K for 3 h. TiO_2 and SiO_2-Al_2O_3 were provided by the Catalysis Society of Japan (JRC-SAL-4 and JRC-TIO-4). Ion-exchange resin was purchased from the Organo Corporation. Ultrapure water was produced using a Thermo Fisher Scientific Barnstead™ Smart2Pure™, with an electrical conductance of 18.2 MΩ cm. $(n\text{-}Bu_4N)[Ir(ppy)_2(CN)_2]$ was synthesized using the reported procedure.[54]

Preparation of Ir–Ni/SiO_2 using $[Ir(CN)_6]^{3-}$ and Ni^{2+} as precursors (**Ir(CN)$_6$-Ni/SiO$_2$-*X***)

A series of Ir–Ni/SiO_2 catalysts using $H_3[Ir(CN)_6]$ and $Ni(NO_3)_2$ as precursors were prepared by the sequential incipient wetness method. The calcined SiO_2 (412 mg) impregnated with an aqueous solution containing $H_3[Ir(CN)_6]$ (0.10 mmol, 330 μL), which was obtained by passing a $K_3[Ir(CN)_6]$ solution through a cation exchange resin, was dried *in vacuo* at room temperature for 1 h. Then, the $H_3[Ir(CN)_6]/SiO_2$ thus achieved was impregnated with an aqueous solution of $Ni(NO_3)_2$ (0.017–0.14 mmol, 330 μL), followed by drying *in vacuo* at room temperature for 1 h. The obtained powder was heated under H_2 (30 mL min^{-1}) at 773 K for 15 min just prior to catalytic tests. The series of catalysts was named **Ir(CN)$_6$**-Ni/SiO_2-*X*, where *X* indicates the amount of Ni relative to the total amounts of Ni and Ir used for the preparation (=Ni/(Ir + Ni)).

Preparation of Ir–Ni/SiO_2 using $[Ir(ppy)_2(CN)_2]^-$ and Ni^{2+} as precursors (**Ir(CN)$_2$-Ni/SiO$_2$-*X***)

Ir–Ni alloy catalysts supported on SiO_2 were prepared by the incipient wetness method similar to the method used for **Ir(CN)$_6$**-Ni/SiO_2-*X*. $[Ir(ppy)_2(CN)_2]^-/SiO_2$ was prepared by impregnation of the calcined SiO_2 (100 mg, calcined at 973 K, 3 h) with an acetonitrile solution of $(n\text{-}Bu_4N)[Ir(ppy)_2(CN)_2]$ (20.8 μmol, 80 μL). After drying *in vacuo* at room temperature for 1 h, $[Ir(ppy)_2(CN)_2]^-/SiO_2$ was then immersed in an acetonitrile solution of $Ni(NO_3)_2$ (3.6–45 μmol, 80 μL), followed by drying *in vacuo* at room temperature for 1 h. The obtained powder was reduced to form an Ir–Ni alloy under H_2 (30 mL min^{-1}) at 773 K for 15 min just prior to use. The series of catalysts was named **Ir(CN)$_2$**-Ni/SiO_2-*X*, where *X* indicates the amount of Ni relative to the total amounts of Ni and Ir used for the preparation (=Ni/(Ir + Ni)).

Preparation of Ir–Ni/SiO_2-Al_2O_3 and Ir–Ni/TiO_2 using $[Ir(ppy)_2(CN)_2]^-$ and Ni^{2+} as precursors (**Ir(CN)$_2$-Ni/M$_A$O$_B$-*X***)

Ir–Ni/SiO_2-Al_2O_3 and Ir–Ni/TiO_2 were prepared by the incipient wetness method used for **Ir(CN)$_2$**-Ni/SiO_2. A support of SiO_2-Al_2O_3 or TiO_2 (70 mg) calcined at 973 K for 3 h prior to use was

impregnated with an acetonitrile solution of (n-Bu_4N)$[Ir(ppy)_2(CN)_2]$ (14.6 μmol, 60 μL), followed by drying *in vacuo* at room temperature for 1 h. Then, Ni was loaded on $[Ir(ppy)_2(CN)_2]^-/SiO_2$-$Al_2O_3$ or TiO_2 by impregnation with an acetonitrile solution of $Ni(NO_3)_2$ (5.31–20.5 μmol, 60 μL), followed by drying *in vacuo* at room temperature for 1 h. The catalysts were reduced under H_2 flow (30 ml min^{-1}) at 773 K for 15 min just before use. The obtained catalysts were named **Ir(CN)$_2$**-Ni/SiO_2-Al_2O_3-*X* or **Ir(CN)$_2$**-Ni/TiO_2-*X*, where *X* indicates the relative amount of Ni to the total amounts of Ni and Ir used for the preparation (=Ni/(Ir + Ni)).

Catalytic activity for styrene hydrogenation

Catalytic activity was investigated in a stainless-steel autoclave with an inserted glass vessel. The typical reaction conditions of styrene hydrogenation were as follows: a reduced catalyst (20 or 50 mg) was added to a mixture of styrene (200 mmol) and methanol (30 g) in a glass vessel in air. Then, the glass vessel sealed in a stainless jacket was heated to 303 K under a pressurized H_2 atmosphere (8 MPa) with magnetic stirring (500 rpm) for a certain time period. After the reaction, the resulting liquid phase was washed with ethanol (10 g). The products were analysed using an FID-GC equipped with a TC–WAX column. The products were quantified by using *n*-dodecane as an internal standard. The initial rates were calculated based on the formed amount of ethylbenzene divided by the reaction times, because no products other than ethylbenzene were detected.

Physical measurements

Powder X-ray diffraction (PXRD) patterns were recorded using a Rigaku MiniFlex 600. Incident X-ray radiation was produced by a Cu X-ray tube operating at 40 kV and 15 mA with Cu K_α radiation (λ = 1.54 Å). The scan rate was 1° min^{-1} from 2θ = 40–48°. Silicon was used as the internal standard, providing the (111) peak at 2θ = 47.46°. X-ray photoelectron spectroscopy (XPS) analyses were performed using a Shimadzu ESCA-3400HSE. The incident radiation was Mg-K_α X-rays (1253.6 eV) at 200 W. The samples were mounted on a stage with double-sided carbon tape. The binding energy of each element was corrected by the C 1s peak (284.6 eV) from the carbon tape. TEM images of nanoparticles mounted on a copper microgrid coated with elastic carbon were obtained using a JEOL JEM-2100 operated at 200 kV with an X-ray energy dispersive (EDX) spectrometer. Particle size was determined by averaging over 100 particles in TEM images. The atomic ratios of Ir and Ni were determined using a Malvern PANalytical Epsilon 1 X-ray fluorescence (XRF) spectrometer.

Results and discussion

In situ formation of Ir(CN)$_6$-Ni and Ir(CN)$_2$-Ni complexes on SiO_2 confirmed by IR spectroscopy

The formation of cyano-bridged complexes was confirmed by mixing Ni^{2+} and $[Ir(CN)_6]^{3-}$ or $[Ir(ppy)_2(CN)_2]^-$ in solution. The IR measurements of the resulting precipitates indicated the higher wavenumber shift of the CN stretching band compared with that of $[Ir(CN)_6]^{3-}$ or $[Ir(ppy)_2(CN)_2]^-$ (Fig. S1†). The CN stretching band of $K_3[Ir(CN)_6]$ that appeared at 2127 cm^{-1} shifted to 2175 cm^{-1} due to the formation of a CN-bridging structure.[55] Similarly, the CN stretching band of (n-Bu_4N)$[Ir(ppy)_2(CN)_2]$ observed at 2092 and 2101 cm^{-1} shifted to 2122 cm^{-1} with a shoulder peak around 2100 cm^{-1} by the reaction with Ni^{2+}. In addition, powder X-ray diffraction (PXRD) for the precipitates obtained by the reaction of $[Ir(CN)_6]^{3-}$ with Ni^{2+} evidenced the formation of cubic structures, so called Prussian blue analogues, with a 3D reticular structure (Fig. S2†). The 1D structure of $[Ir(ppy)_2(CN)_2]^-$ with Ni^{2+} is appropriate under consideration of the molecular structure; however, further investigation is necessary.

A series of coordination polymers containing Ir and Ni with different Ni/Ir ratios was supported on SiO_2 surfaces by the two-step impregnation method where $[Ir(CN)_6]^{3-}$ was impregnated first and then $Ni(NO_3)_2$ in SiO_2, because simple one-step impregnation may result in the formation of insoluble coordination polymers apart from the SiO_2 surfaces. The *in situ* formation of a coordination polymer was confirmed by IR measurements (Fig. 1). The CN stretching band, ν(CN), of $[Ir(CN)_6]^{3-}$ supported on SiO_2 (**Ir(CN)$_6$**/SiO_2) appeared at the same position as $K_3[Ir(CN)_6]$ at 2129 cm^{-1} (Fig. 1a).[55] The impregnation of an aqueous $Ni(NO_3)_2$ solution with **Ir(CN)$_6$**/

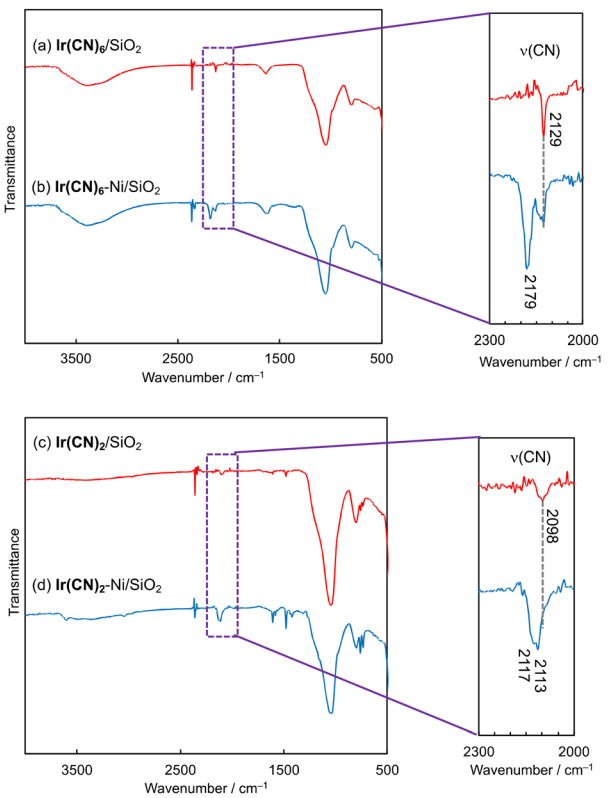

Fig. 1 IR spectra of (a) **Ir(CN)$_6$**/SiO_2, (b) **Ir(CN)$_6$**-Ni/SiO_2-0.15, (c) **Ir(CN)$_2$**/SiO_2 and (d) **Ir(CN)$_2$**-Ni/SiO_2.

SiO_2, in which the ratio of Ni/(Ir + Ni) = 0.15, provided a new ν(CN) at 2179 cm^{-1} (Fig. 1b). Such a high wavenumber shift of ν(CN) is generally observed when the CN bridging structure forms;[55] thus, the coordination polymer with an Ir–CN–Ni bridged structure formed on the SiO_2 surfaces. Such a high wavenumber shift of ν(CN) was also observed when $[Ir(ppy)_2(CN)_2]^-/SiO_2$ (**Ir(CN)$_2$**/SiO_2) was impregnated with $Ni(NO_3)_2$, where the ν(CN) shifted to 2113 and 2117 cm^{-1} from the 2098 cm^{-1} observed for **Ir(CN)$_2$**/SiO_2 alone (Fig. 1c and d). Therefore, the two-step impregnation method allowed the formation of cyano-bridged coordination polymers containing Ir^{3+} and Ni^{2+} on SiO_2. The cyano-bridged coordination polymers thus formed were reduced by H_2 at higher temperatures to achieve Ir–Ni alloys.

Compositions and sizes of Ir–Ni alloy particles in Ir(CN)$_6$-Ni/SiO_2-*X*

The loading amounts of Ir were fixed to 4.6% of SiO_2 in a series of **Ir(CN)$_6$**-Ni/SiO_2-*X* where *X* represents the amounts of Ni relative to the total amounts of Ir and Ni [=Ni/(Ir + Ni)] in moles. The values of *X* determined by XRF were almost the same as expected from the used amounts of Ni and Ir precursors (Table 1). Then, the Ni contents in Ir–Ni alloys of a series of catalysts were estimated by powder X-ray diffraction (PXRD) (Fig. 2 and S3†). The (111) peak of Ir metal appearing at 40.70° was shifted to a higher angle (between 40.7° and 41.0°) by increasing *X*, indicating that the Ir–Ni alloys readily formed. The Ni contents in Ir–Ni alloys estimated from Vegard's law are tabulated in Table 1 together with the relative Ni amounts determined by XRF. The Ni contents in Ir–Ni alloys estimated from Vegard's law were almost the same as the *X* values for **Ir(CN)$_6$**-Ni/SiO_2-*X* with *X* = 0.05–0.15. However, no further increase of Ni contents in Ir–Ni alloys was observed with *X* values higher than 0.20. The maximum Ni content of 0.14 in Ir–Ni alloys implied that one Ni^{2+} ion was mainly surrounded by six $[Ir(CN)_6]^{3-}$, in which Ni/(Ir + Ni) was 0.14 (=1/(1 + 6)). No appearance of PXRD peaks assignable to Ni metal implied that Ni^{2+} ions not bound to $[Ir(CN)_6]^{3-}$ were atomically dispersed on the SiO_2 support or the formed amorphous phase.

The Ir–Ni alloys formed on SiO_2 were observed by TEM. The sizes estimated by Scherrer's equation were as large as ~50 nm based on the peak appearing around 40.70° in PXRD. TEM observations of **Ir(CN)$_6$**-Ni/SiO_2-0.20 indicated that the sizes of the Ir–Ni alloys were widely distributed from 5 to 70 nm (Fig. 3 and S4a†). Thus, the size of the Ir–Ni alloy nanoparticles was hardly controlled by using $[Ir(CN)_6]^{3-}$ as a precursor although the compositions could be well controlled.

The composition uniformity of Ir–Ni alloy particles was further confirmed by the EDX line spectra for multiple single particles in TEM observations. The Ni contents in the three single particles of **Ir(CN)$_6$**-Ni/SiO_2-0.4 were 0.17, 0.19 and 0.13, which were close to the maximum Ni content of 0.14 determined by PXRD measurements (Fig. S5†). The frequency of smaller particles in **Ir(CN)$_6$**-Ni/SiO_2-0.4 increased compared with that in **Ir(CN)$_6$**-Ni/SiO_2-0.2, suggesting that excess Ni formed unalloyed small Ni particles (Fig. S4†).

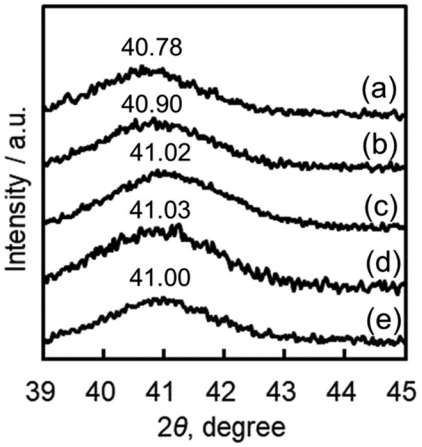

Fig. 2 Powder X-ray diffraction peaks of **Ir(CN)$_6$**-Ni/SiO_2-*X* [*X* = Ni/(Ni + Ir)] in the Ir(111) region. *X* = (a) 0.05, (b) 0.10, (c) 0.15, (d) 0.20 and (e) 0.25.

Table 1 The relative amounts of Ni to the total amounts of (Ir + Ni) in Ir(CN)$_6$-Ni/SiO_2-*X* determined by XRF, Ni contents in Ir–Ni alloys in Ir(CN)$_6$-Ni/SiO_2-*X* determined by PXRD, and the positions of PXRD peaks appearing around 40.70° assignable to the Ir(111) peak

	Ni/(Ir + Ni)		
Catalyst	XRF	PXRD	Peak position (2θ / °)
Ir(CN)$_6$-Ni/SiO_2-0.05	0.05	0.05	40.78
Ir(CN)$_6$-Ni/SiO_2-0.10	0.11	0.10	40.90
Ir(CN)$_6$-Ni/SiO_2-0.15	0.15	0.14	41.02
Ir(CN)$_6$-Ni/SiO_2-0.20	0.19	0.14	41.03
Ir(CN)$_6$-Ni/SiO_2-0.25	0.25	0.14	41.00

Catalytic activity of Ir(CN)$_6$-Ni/SiO_2-*X* for styrene hydrogenation

The catalytic activity of **Ir(CN)$_6$**-Ni/SiO_2-*X* was evaluated for styrene hydrogenation performed in an autoclave at 303 K for 15–60 min under a pressurised hydrogen atmosphere (8 MPa) (Fig. 4a). No products other than ethylbenzene were detected in solution. The concentrations of the formed ethylbenzene were linearly increased up to 60 min for a series of **Ir(CN)$_6$**-Ni/SiO_2-*X* (Fig. 4b).

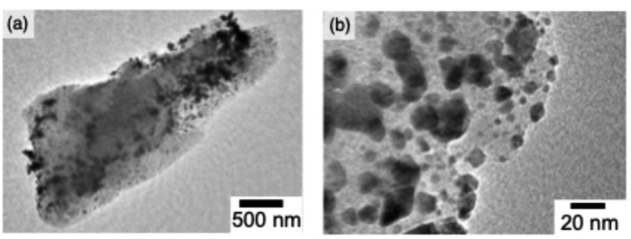

Fig. 3 Transmission electron microscope (TEM) images of **Ir(CN)$_6$**-Ni/SiO_2-0.20 in (a) wide and (b) magnified views.

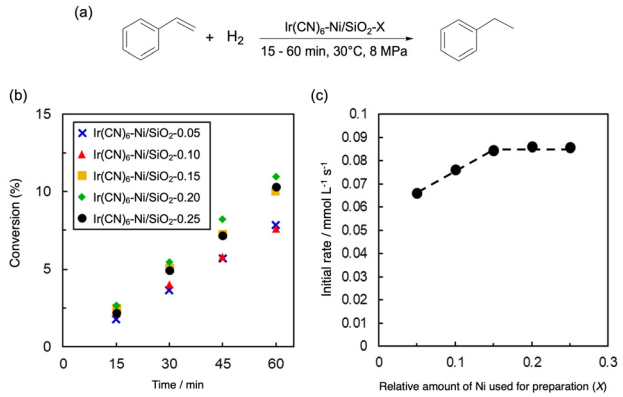

Fig. 4 (a) Reaction conditions of catalytic styrene hydrogenation. Catalytic activity of **Ir(CN)$_6$**-Ni/SiO$_2$-*X* for styrene hydrogenation. (b) Time courses of **Ir(CN)$_6$**-Ni/SiO$_2$-0.05 (×), **Ir(CN)$_6$**-Ni/SiO$_2$-0.10 (▲), **Ir(CN)$_6$**-Ni/SiO$_2$-0.15 (■), **Ir(CN)$_6$**-Ni/SiO$_2$-0.20 (◆) and **Ir(CN)$_6$**-Ni/SiO$_2$-0.25 (●). (c) Initial reaction rates (<60 min) plotted against the relative amounts of Ni used for the preparation (*X*).

The initial rates determined from the slopes of the plots (=formed ethylbenzene concentrations divided by reaction times) increased with increasing the *X* of **Ir(CN)$_6$**-Ni/SiO$_2$-*X* up to 0.15, while no further increase was observed when *X* was higher than 0.15 (Fig. 4c). Therefore, an increase of Ni contents in the Ir–Ni alloy is critical to achieve catalytic activity, and unalloyed Ni species deposited on SiO$_2$ are inactive for the reaction.[26] Further increase of Ni contents to higher than 0.15 in the Ir–Ni alloys is promising to enhance the catalytic activity.

Furthermore, the ethylbenzene formation rates lower than 0.09 mmol L^{-1} s^{-1} with **Ir(CN)$_6$**-Ni/SiO$_2$-*X* catalysts were inferior to that observed with Ir–Ni/SiO$_2$ prepared by a conventional impregnation method, 0.52 mmol L^{-1} s^{-1},[41] because of the larger sizes of the Ir–Ni particles. The formation of larger particles was partly due to the easy formation of coordination polymers with a 3D reticular structure at higher Ni contents. Therefore, an Ir precursor to form a non-reticular structure with Ni^{2+} seems to be promising to reduce the size of Ir–Ni nanoparticles. [Ir(ppy)$_2$(CN)$_2$] (ppy = 2-phenylpyridine) would be an appropriate candidate because only two CN$^-$ ligands are available for polymerization with Ni^{2+} (Scheme 2b). The ppy chelate ligand strongly directs the formation of 1D polymer chains by disturbing the formation of a 3D reticular structure.

Compositions and particles sizes of Ir–Ni alloy particles in Ir(CN)$_2$-Ni/SiO$_2$-*X*

A series of **Ir(CN)$_2$**-Ni/SiO$_2$-*X* catalysts was prepared by using [Ir(ppy)$_2$(CN)$_2$]$^-$ as a precursor for reducing the particle sizes of Ir–Ni alloys. The values of *X* determined by XRF agreed well with the used amounts of Ir and Ni precursors within experimental error for a series of **Ir(CN)$_2$**-Ni/SiO$_2$-*X* (Table 2). PXRD measurements of the series of catalysts indicated that the peaks appearing around 41° became broader compared with those of **Ir(CN)$_6$**-Ni/SiO$_2$-*X* (Fig. 5 and S6†). Two possible reasons for the peak broadening are the formation of small-sized crystallites and alloy formation with gradually changed

Table 2 The amounts of Ni relative to the total amounts of (Ir + Ni) in **Ir(CN)$_2$**-Ni/SiO$_2$-*X* determined by XRF, Ni contents in Ir–Ni alloys in **Ir(CN)$_2$**-Ni/SiO$_2$-*X* determined by PXRD, the positions of PXRD peaks appearing around 40.70° assignable to the Ir(111) peak, and particles sizes estimated from the PXRD line width

Catalysts	Ni/(Ir + Ni) XRF	Ni/(Ir + Ni) PXRD	Peak position (2θ /°)	Particle size/nm
Ir(CN)$_2$-Ni/SiO$_2$-0.05	0.05	0.07	41.00	9.0
Ir(CN)$_2$-Ni/SiO$_2$-0.1	0.10	0.11	41.11	6.8
Ir(CN)$_2$-Ni/SiO$_2$-0.15	0.14	0.15	41.32	1.9
Ir(CN)$_2$-Ni/SiO$_2$-0.2	0.18	0.20	41.53	2.8
Ir(CN)$_2$-Ni/SiO$_2$-0.3	0.29	0.29	41.89	10.1
Ir(CN)$_2$-Ni/SiO$_2$-0.4	0.38	0.25	41.72	8.1

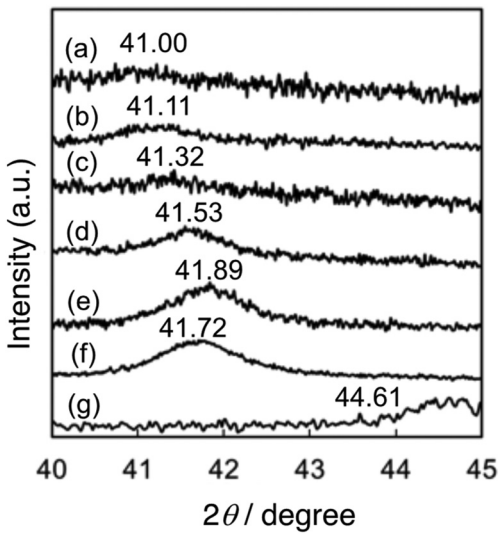

Fig. 5 Powder X-ray diffraction peaks of (a) **Ir(CN)$_2$**-Ni/SiO$_2$-0.05, (b) **Ir(CN)$_2$**-Ni/SiO$_2$-0.10, (c) **Ir(CN)$_2$**-Ni/SiO$_2$-0.15, (d) **Ir(CN)$_2$**-Ni/SiO$_2$-0.20, (e) **Ir(CN)$_2$**-Ni/SiO$_2$-0.3, (f) **Ir(CN)$_2$**-Ni/SiO$_2$-0.4 and (g) Ni/SiO$_2$ as a reference, in the Ir(111) region.

compositions. The particle sizes of the Ir–Ni alloys in a series of **Ir(CN)$_2$**-Ni/SiO$_2$-*X* estimated by Scherrer's equation were smaller than ~10 nm, although the particle size depends on the *X* value. For example, the estimated sizes of the Ir–Ni alloys of **Ir(CN)$_2$**-Ni/SiO$_2$-0.10 and -0.15 were as small as 6.8 and 1.9 nm, respectively. The average particle sizes of Ir–Ni alloys confirmed by the TEM observation were ~8.5(±4.4) and ~4.4(±2.4) nm, respectively (Fig. 6 and S7†). The small difference in the sizes determined by PXRD and TEM for each sample demonstrates the homogeneity of Ir–Ni alloy compositions. The Ni contents in Ir–Ni alloys were estimated by PXRD (Table 2 and Fig. 5). The maximum Ni concentration in the Ir–Ni alloys estimated from Vegard's law reached 0.29, which is double that obtained for the catalyst prepared by using [Ir(CN)$_6$]$^{3-}$ and Ni^{2+} as precursors. The maximum Ni contents suggested the formation of linear Ni[Ir(ppy)$_2$(CN)$_2$]$_2$, in which the maximum theoretical Ni content was 0.33. The *in situ* formation of the one-dimensional coordination polymer

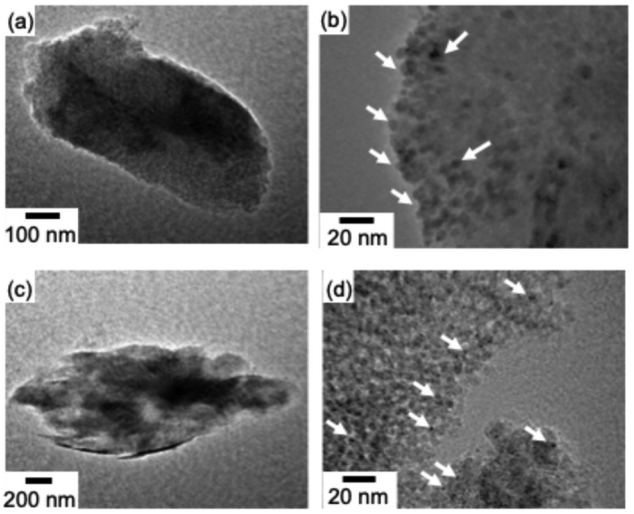

Fig. 6 Transmission electron microscope (TEM) images of (a and b) **Ir(CN)$_2$**-Ni/SiO$_2$-0.1 and (c and d) **Ir(CN)$_2$**-Ni/SiO$_2$-0.15. The white arrows indicate the Ir–Ni particles. The white arrows indicate the Ir–Ni alloy particles.

is beneficial not only for reducing the size of Ir–Ni alloy nanoparticles but also for increasing the maximum Ni contents in the Ir–Ni alloy.

The Ni contents of three single particles of **Ir(CN)$_2$**-Ni/SiO$_2$-0.4 were 0.23, 0.22 and 0.24, which were close to the 0.25 determined by PXRD measurements (Fig. S8†). The formation of particles larger than 12 nm was rarely observed in **Ir(CN)$_2$**-Ni/SiO$_2$-0.4, also supporting the formation of smaller Ni particles (Fig. 7). These results suggest that the Ir–Ni particles formed on SiO$_2$ surfaces have uniform Ni contents, and the excess Ni formed tiny Ni particles.

Catalysis evaluation of Ir(CN)$_2$-Ni/SiO$_2$-*X* for styrene hydrogenation

The catalytic activity of a series of **Ir(CN)$_2$**-Ni/SiO$_2$-*X* was evaluated for styrene hydrogenation. The initial rates were determined from the ethylbenzene formation rates for 60 min (Fig. 7). The maximum initial reaction rates increased to almost double those of **Ir(CN)$_6$**-Ni/SiO$_2$-*X*. The higher catalytic activity of **Ir(CN)$_2$**-Ni/SiO$_2$-*X* compared with that of **Ir(CN)$_6$**-Ni/SiO$_2$-*X* indicates that the smaller size of Ir–Ni alloy particles is beneficial for achieving high catalytic activity. The initial rate became higher with increasing the Ni contents in the Ir–Ni alloy up to 0.20, reaching the maximum initial rate of 0.16 mmol L^{-1} s^{-1} (Fig. 7b). However, the initial rates decreased at higher Ni contents in the Ir–Ni alloys. The higher Ni contents could reduce the number of isolated Ni atoms on Ir metal surfaces.[44]

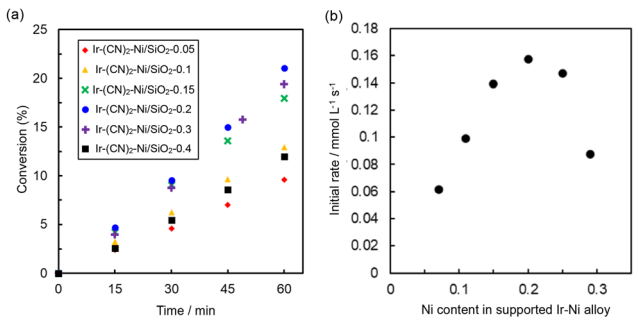

Fig. 7 Catalytic activity of **Ir(CN)$_2$**-Ni/SiO$_2$-*X* for styrene hydrogenation. (a) Time course of styrene conversion catalysed by **Ir(CN)$_2$**-Ni/SiO$_2$-0.05 (◆), **Ir(CN)$_2$**-Ni/SiO$_2$-0.1 (▲), **Ir(CN)$_2$**-Ni/SiO$_2$-0.2 (×), **Ir(CN)$_2$**-Ni/SiO$_2$-0.2 (●), **Ir(CN)$_2$**-Ni/SiO$_2$-0.3 (+) and **Ir(CN)$_2$**-Ni/SiO$_2$-0.4 (■). (b) Initial rates as a function of Ni contents (=Ni/(Ir + Ni)) in the Ir–Ni alloys determined by PXRD.

Support effect of Ir(CN)$_2$-Ni/M$_A$O$_B$-*X*

The particle sizes were rather small for **Ir(CN)$_2$**-Ni/SiO$_2$ compared with **Ir(CN)$_6$**-Ni/SiO$_2$; however, the enhancement of the initial rate was less than double, indicating that a strong support effect can be expected for smaller Ir–Ni nanoparticles. Thus, Ir–Ni alloys loaded on other supports, M$_A$O$_B$ (SiO$_2$-Al$_2$O$_3$ or TiO$_2$), were examined for a series of catalysts prepared with [Ir(ppy)$_2$(CN)$_2$]$^-$ as a precursor. The PXRD measurements for a series of **Ir(CN)$_2$**-Ni/M$_A$O$_B$-*X* indicated that the Ni concentrations in Ir–Ni alloys estimated by Vegard's law agreed with those expected from the amounts used for the catalyst preparation (Fig. 8). The Ni contents in Ir–Ni alloys are summarised in Table 3, although the diffraction peaks were broad for **Ir(CN)$_2$**-Ni/SiO$_2$-Al$_2$O$_3$-*X*. The nanoparticles of Ir–Ni alloys formed on **Ir(CN)$_2$**-Ni/SiO$_2$-Al$_2$O$_3$-0.2 and **Ir(CN)$_2$**-Ni/TiO$_2$-0.2 were observed by TEM as shown in Fig. 9. The Ir–Ni alloys formed on each support are indicated by the white arrows. The Ir–Ni alloys are tiny nanoparticles smaller than 2 nm in **Ir(CN)$_2$**-Ni/SiO$_2$-Al$_2$O$_3$-0.2. The average particle size is 5.1(±2.6) nm as estimated from the TEM image of Ir–Ni/SiO$_2$-Al$_2$O$_3$-0.2 (Fig. 9a and S9†). The size is almost the same as that calculated using the Scherrer equation with the PXRD peak width. In addition, islands smaller than 20 nm were observed for **Ir**

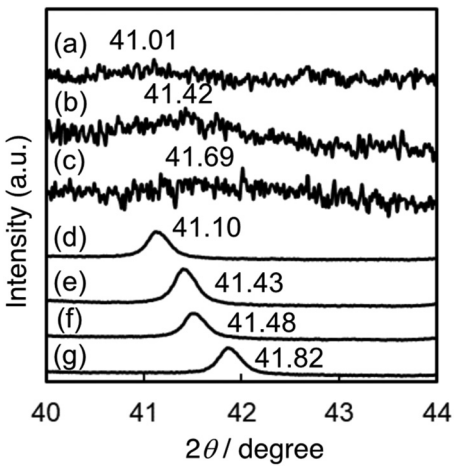

Fig. 8 Powder X-ray diffraction peaks of **Ir(CN)$_2$**-Ni/M$_A$O$_B$-*X* [M$_A$O$_B$-*X* = (a) SiO$_2$-Al$_2$O$_3$-0.1, (b) SiO$_2$-Al$_2$O$_3$-0.2, (c) SiO$_2$-Al$_2$O$_3$-0.3, (d) TiO$_2$-0.1, (e) TiO$_2$-0.2, (f) TiO$_2$-0.21, and (g) TiO$_2$-0.3] in the Ir(111) region.

Table 3 The amounts of Ni relative to the total amounts of (Ir + Ni) in **Ir(CN)$_2$**-Ni/M_AO_B-*X* determined by XRF, Ni contents in Ir–Ni alloys in **Ir(CN)$_2$**-Ni/M_AO_B-*X* determined by PXRD, and the positions of PXRD peaks appearing around 40.70° assignable to the Ir(111) peak

	Ni/(Ir + Ni)		
Catalyst	XRF	PXRD	Peak position (2θ /°)
Ir(CN)$_2$-Ni/SiO_2-Al_2O_3-0.1	0.10	0.10	41.01
Ir(CN)$_2$-Ni/SiO_2-Al_2O_3-0.2	0.20	0.18	41.42
Ir(CN)$_2$-Ni/SiO_2-Al_2O_3-0.3	0.30	0.28	41.48
Ir(CN)$_2$-Ni/TiO_2-0.1	0.10	0.11	41.13
Ir(CN)$_2$-Ni/TiO_2-0.18	0.20	0.18	41.43
Ir(CN)$_2$-Ni/TiO_2-0.21	0.21	0.21	41.32
Ir(CN)$_2$-Ni/TiO_2-0.3	0.30	0.29	41.53

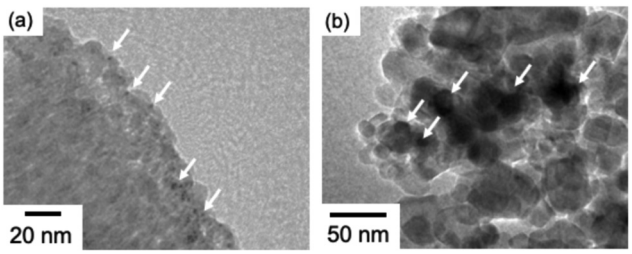

Fig. 9 Transmission electron microscopy (TEM) images of (a) **Ir(CN)$_2$**-Ni/SiO_2-Al_2O_3-0.2 and (b) **Ir(CN)$_2$**-Ni/TiO_2-0.20. The white arrows indicate the Ir–Ni alloy particles.

(CN)$_2$-Ni/TiO_2-0.2 (Fig. 9b). Thus, Ir–Ni alloys with precisely controlled compositions and small sizes were obtained by using $[Ir(ppy)_2(CN)_2]^-$ as a precursor regardless of supports.

Catalysis of Ir(CN)$_2$-Ni/M_AO_B-*X* for styrene hydrogenation

The catalytic activity of **Ir(CN)$_2$**-Ni/M_AO_B-*X* was evaluated for styrene hydrogenation. The initial rate calculated from the conversions for 60 min became the maximum at a Ni concentration of around 0.2 (Fig. 10). Such a volcano-type relationship between the initial rate and the Ni contents in Ir–Ni alloys is similar to that observed for **Ir(CN)$_2$**-Ni/SiO_2-*X*, although **Ir(CN)$_2$**-Ni/SiO_2-*X* catalysts were more active than **Ir(CN)$_2$**-Ni/SiO_2-Al_2O_3-*X* and **Ir(CN)$_2$**-Ni/TiO_2-*X*. In particular, the catalytic activity of **Ir(CN)$_2$**-Ni/TiO_2-*X* was much lower than those of **Ir(CN)$_2$**-Ni/SiO_2-*X* and **Ir(CN)$_2$**-Ni/SiO_2-Al_2O_3-*X*. The lower catalytic activity seemed to be due to larger island sizes; however, Ir–Ni alloy particles in **Ir(CN)$_6$**-Ni/SiO_2-*X* larger than 50 nm showed a certain activity. Therefore, the electronic states of Ir and Ni on TiO_2 and SiO_2 seemed to be more important than particle sizes.

The electronic states of Ir and Ni were investigated by X-ray photoelectron spectroscopy (XPS). The XPS measurements of **Ir(CN)$_2$**-Ni/SiO_2-0.20 revealed that Ir $4f_{7/2}$ and Ir $4f_{5/2}$ peaks appeared at 60.8 and 63.7 eV (Fig. 11a). The binding energy for Ir $4f_{7/2}$ lower than 61 eV evidenced that the Ir species are in the metallic state.[56] Also, Ni $2p_{3/2}$ and Ni $2p_{1/2}$ peaks of **Ir(CN)$_2$**-Ni/SiO_2-0.20 appeared at 855.1 and 872.3 eV (Fig. 11b). The peak separation of 17.2 eV is close to that reported for Ni

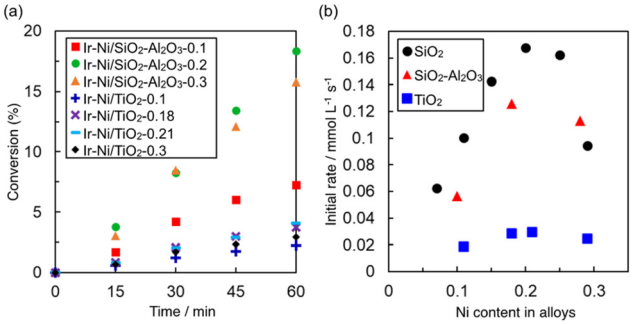

Fig. 10 (a) Time profiles of styrene conversion in styrene hydrogenation catalysed by **Ir(CN)$_2$**-Ni/SiO_2-Al_2O_3-*X* (*X* = 0.1 (■), 0.2 (●) and 0.3 (▲)) and **Ir(CN)$_2$**-Ni/TiO_2-*X* (*X* = 0.1 (+), 0.18 (×), 0.21 (–) and 0.3 (◆)) at 30 °C under H_2 (8 MPa). (b) Initial rates for ethylbenzene formation as a function of Ni concentrations (=Ni/(Ir + Ni)) in Ir–Ni alloys of **Ir(CN)$_2$**-Ir/MOx (MOx = SiO_2 (●), SiO_2-Al_2O_3 (▲) and TiO_2 (■)).

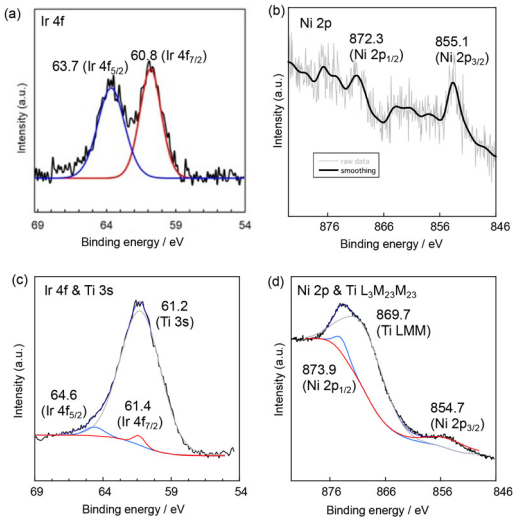

Fig. 11 XPS spectra of Ir 4f and Ni 2p regions of (a and b) **Ir(CN)$_2$**-Ni/SiO_2-0.20 and (c and d) **Ir(CN)$_2$**-Ni/TiO_2-0.20.

metal, 17.4 eV, rather than the 18.4 eV reported for NiO.[56] However, the binding energy for $2p_{3/2}$ is more positive than that reported for Ni metal as 852.3 eV by 2.8 eV. Usually, such a high binding energy shift indicates the species are in higher oxidation states; however, intense satellite peaks characteristic for NiO species are missing. Therefore, the Ni species of **Ir(CN)$_2$**-Ni/SiO_2-0.20 are metallic but positively charged due to the higher electronegativity of Ir metal (2.22) than that of Ni metal (1.91).[57]

Deconvolution of the overlapped Ir 4f and Ti 3s peaks of **Ir(CN)$_2$**-Ni/TiO_2-0.20 indicated that Ir $4f_{7/2}$ and Ir $4f_{5/2}$ peaks appeared at 61.4 and 64.6 eV (Fig. 11c). The Ir 4f peaks were shifted to a higher binding energy region by 0.6 and 0.9 eV compared with those of Ir $4f_{7/2}$ and $4f_{5/2}$ of **Ir(CN)$_2$**-Ni/SiO_2-0.20, indicating that the Ir metal on TiO_2 is in a higher oxidation state than that on SiO_2. The catalytic role of Ir metal has been reported as providing hydrogen atoms to an

adsorbed styrene on a Ni atom.[44] The electron deficient state of Ir results in deceleration of the dissociation of hydrogen molecules to hydrogen atoms. The Ni $2p_{3/2}$ peak of **Ir(CN)$_2$**-Ni/TiO_2-0.20 appears at 854.7 eV, which is lower than that of **Ir(CN)$_2$**-Ni/SiO_2-0.20 by 0.4 eV. The peak position of Ni $2p_{1/2}$ was uncertain due to overlapping with the Ti $L_3M_{23}M_{23}$ Auger peak; however, the Ni in **Ir(CN)$_2$**-Ni/TiO_2-0.20 is more negatively charged than that on SiO_2. The observed strong support effects could result from the electronic state change occurring in Ir–Ni alloys.

Conclusions

Ir–Ni alloy catalysts with precisely controlled compositions were prepared on SiO_2 by using $[Ir(CN)_6]^{3-}$ or $[Ir(ppy)_2(CN)_2]^-$ as an Ir precursor. Ni^{2+} was alloyed after reduction of *in situ* formed coordination polymers on the support. However, the maximum Ni contents in Ir–Ni alloys were limited to 0.14 and 0.29 with $[Ir(CN)_6]^{3-}$ and $[Ir(ppy)_2(CN)_2]^-$, respectively, because of compositions of coordination polymers thus formed. The particles sizes of Ir–Ni alloys using $[Ir(ppy)_2(CN)_2]^-$ as the precursor were smaller than those using $[Ir(CN)_6]^{3-}$, indicating that a one-dimensional structure is more suitable to prepare smaller Ir–Ni particles than a three dimensional structure. The reduction of Ir–Ni particles sizes enhanced the catalytic activity for styrene hydrogenation. The precise control of compositions and sizes of Ir–Ni particles was also possible for TiO_2 and SiO_2-Al_2O_3 supports. Thus, an appropriate choice of coordination polymers as precursors allows control of the compositions and sizes of alloy nanoparticles on metal oxide supports.

Author contributions

Y.Y.: conceptualization, methodology, writing – original draft, and writing – review and editing. M.N.: investigation, methodology, and writing – review and editing. T. Nakabayashi: investigation, methodology, and writing – review and editing. T. Nakazono: investigation, methodology, and writing – review and editing. H. L.: investigation, methodology, and writing – review and editing. P. C.: investigation, methodology, and writing – review and editing. M. T.: conceptualization, methodology, and writing – review and editing.

Data availability

Supporting data of this study are available within the paper. Further details regarding the data are available from the corresponding author upon reasonable request.

Conflicts of interest

There are no conflicts to declare.

Acknowledgements

This work was supported by the Grant-in-Aid for Scientific Research (B) (grant 22H01871) and (C) (grant 23K04770) and the Grant-in-Aid for Specially Promoted Research (23H05404) from the JSPS, University fellowship creation project for creating scientific and technological innovation (JPMJFS2138) from JST, and Strategic Reserach Promotion Project (Priority Research) 2024 from Osaka Metropolitan University.

References

1 T. Li, D. Jia, S. Zhou, Z. Liu, J. Chen, T. Ban, A. Li, H. Li and H. Gao, *Fuel*, 2024, **373**, 132329.
2 D. Zhao, X. Li, K. Zhang, J. Guo, X. Huang and G. Wang, *Coord. Chem. Rev.*, 2023, **487**, 215159.
3 J.-Y. Yan and G.-P. Cao, *Macromolecules*, 2023, **56**, 3774–3808.
4 A. N. Marianov, Y. Jiang, A. Baiker and J. Huang, *Chem. Catal.*, 2023, **3**, 100631.
5 B. Lakshminarayana, M. Selvaraj, G. Satyanarayana and C. Subrahmanyam, *Catal. Rev.*, 2022, **66**, 259–342.
6 K. Liu, R. Qin and N. Zheng, *J. Am. Chem. Soc.*, 2021, **143**, 4483–4499.
7 L. Zhang, M. Zhou, A. Wang and T. Zhang, *Chem. Rev.*, 2020, **120**, 683–733.
8 M. A. Stoffels, F. J. R. Klauck, T. Hamadi, F. Glorius and J. Leker, *Adv. Synth. Catal.*, 2020, **362**, 1258–1274.
9 X. Lan and T. Wang, *ACS Catal.*, 2020, **10**, 2764–2790.
10 S. Zhang, J. Li, Z. Xia, C. Wu, Z. Zhang, Y. Ma and Y. Qu, *Nanoscale*, 2017, **9**, 3140–3149.
11 P. Liu, Y. Zhao, R. Qin, S. Mo, G. Chen, L. Gu, D. M. Chevrier, P. Zhang, Q. Guo, D. Zang, B. Wu, G. Fu and N. Zheng, *Science*, 2016, **352**, 797–801.
12 Y. Wu, S. Cai, D. Wang, W. He and Y. Li, *J. Am. Chem. Soc.*, 2012, **134**, 8975–8981.
13 H. Wang, A. M. Fiore, C. Fliedel, E. Manoury, K. Philippot, M. M. Dell'Anna, P. Mastrorilli and R. Poli, *Nanoscale Adv.*, 2021, **3**, 2554–2566.
14 M. Tamura, N. Hayashigami, A. Nakayama, Y. Nakagawa and K. Tomishige, *ACS Catal.*, 2021, **12**, 868–876.
15 L. M. Martínez-Prieto, I. Cano and P. W. N. M. van Leeuwen, in *Iridium Catalysts for Organic Reactions*, ed. L. A. Oro and C. Claver, Springer International Publishing, 2021, pp. 397–454.
16 S. Hanf, L. A. Rupflin, R. Gläser and S. Schunk, *Catalysts*, 2020, **10**, 510.
17 F. Corvaisier, Y. Schuurman, A. Fecant, C. Thomazeau, P. Raybaud, H. Toulhoat and D. Farrusseng, *J. Catal.*, 2013, **307**, 352–361.
18 P. Buchwalter, J. Rose and P. Braunstein, *Chem. Rev.*, 2015, **115**, 28–126.
19 D. C. Zhong, Y. N. Gong, C. Zhang and T. B. Lu, *Chem. Soc. Rev.*, 2023, **52**, 3170–3214.

20 X. Cai, H. Wang, Y. Tian, W. Ding and Y. Zhu, *ACS Catal.*, 2024, **14**, 11918–11930.
21 L. B. Belykh, N. I. Skripov, T. P. Sterenchuk, T. A. Kornaukhova, E. A. Milenkaya and F. K. Schmidt, *Mol. Catal.*, 2022, **528**, 112509.
22 A. K. Singh and Q. Xu, *ChemCatChem*, 2013, **5**, 652–676.
23 R. Ferrando, J. Jellinek and R. L. Johnston, *Chem. Rev.*, 2008, **108**, 845–910.
24 Z. P. Wu, S. Shan, S. Q. Zang and C. J. Zhong, *Acc. Chem. Res.*, 2020, **53**, 2913–2924.
25 K. Murugesan, V. G. Chandrashekhar, C. Kreyenschulte, M. Beller and R. V. Jagadeesh, *Angew. Chem., Int. Ed.*, 2020, **59**, 17408–17412.
26 M. B. Gawande, A. Goswami, T. Asefa, H. Guo, A. V. Biradar, D. L. Peng, R. Zboril and R. S. Varma, *Chem. Soc. Rev.*, 2015, **44**, 7540–7590.
27 Q. Zhang, I. Lee, J. B. Joo, F. Zaera and Y. Yin, *Acc. Chem. Res.*, 2013, **46**, 1816–1824.
28 J. Kim, H. E. Kim and H. Lee, *ChemSusChem*, 2018, **11**, 104–113.
29 L. Liu and A. Corma, *Trends Chem.*, 2020, **2**, 383–400.
30 J. Han, J. Lu, M. Wang, Y. Wang and F. Wang, *Chin. J. Chem.*, 2019, **37**, 977–988.
31 G. Giannakakis, M. Flytzani-Stephanopoulos and E. C. H. Sykes, *Acc. Chem. Res.*, 2019, **52**, 237–247.
32 M. T. Darby, R. Réocreux, E. C. H. Sykes, A. Michaelides and M. Stamatakis, *ACS Catal.*, 2018, **8**, 5038–5050.
33 X. F. Yang, A. Wang, B. Qiao, J. Li, J. Liu and T. Zhang, *Acc. Chem. Res.*, 2013, **46**, 1740–1748.
34 G. Kyriakou, M. B. Boucher, A. D. Jewell, E. A. Lewis, T. J. Lawton, A. E. Baber, H. L. Tierney, M. Flytzani-Stephanopoulos and E. C. Sykes, *Science*, 2012, **335**, 1209–1212.
35 H. Zhang, T. Watanabe, M. Okumura, M. Haruta and N. Toshima, *Nat. Mater.*, 2011, **11**, 49–52.
36 R. T. Hannagan, G. Giannakakis, M. Flytzani-Stephanopoulos and E. C. H. Sykes, *Chem. Rev.*, 2020, **120**, 12044–12088.
37 H. Feng, W. Liu, L. Wang, E. Xu, D. Pang, Z. Ren, S. Wang, S. Zhao, Y. Deng, T. Liu, Y. Yang, X. Zhang, F. Li and M. Wei, *Adv. Sci.*, 2024, **11**, e2304908.
38 Y. Chen, R. Zhang, Z. Chen, J. Liao, X. Song, X. Liang, Y. Wang, J. Dong, C. V. Singh, D. Wang, Y. Li, F. D. Toste and J. Zhao, *J. Am. Chem. Soc.*, 2024, **146**, 10847–10856.
39 Z. Wang, X. Zhou, G. Wang, Q. Tong, H. Wan and L. Dong, *Inorg. Chem.*, 2024, **63**, 7241–7254.
40 H. Yu, W. Tang, K. Li, S. Zhao, H. Yin and S. Zhou, *ACS Appl. Mater. Interfaces*, 2019, **11**, 6958–6969.
41 J.-q. Bai, M. Tamura, Y. Nakagawa and K. Tomishige, *Chem. Commun.*, 2019, **55**, 10519–10522.
42 Z. Zhou, T. Zeng, Z. Cheng and W. Yuan, *Ind. Eng. Chem. Res.*, 2010, **49**, 11112–11118.
43 T. A. Nijhuis, F. M. Dautzenberg and J. A. Moulijn, *Chem. Eng. Sci.*, 2003, **58**, 1113–1124.
44 J.-q. Bai, M. Tamura, A. Nakayama, Y. Nakagawa and K. Tomishige, *ACS Catal.*, 2021, **11**, 3293–3309.
45 H. Yang, J. Liu, Z. Chen, R. Wang, B. Fei, H. Liu, Y. Guo and R. Wu, *Chem. Eng. J.*, 2021, **420**, 127671.
46 T. G. U. Ghobadi, E. Ozbay and F. Karadas, *Chem. – Eur. J.*, 2021, **27**, 3638–3649.
47 H. Matsuoka, O. Tomita, H. Tabe, H. Suzuki, Y. Yamada and R. Abe, *J. Photochem. Photobiol., A*, 2022, **426**, 113753.
48 Y. Yamada, K. Oyama, R. Gates and S. Fukuzumi, *Angew. Chem., Int. Ed.*, 2015, **54**, 5613–5617.
49 Y. Yamada, K. Oyama, T. Suenobu and S. Fukuzumi, *Chem. Commun.*, 2017, **53**, 3418–3421.
50 M. Yamane, H. Tabe, M. Kawakami, H. Tanaka, T. Kawamoto and Y. Yamada, *Inorg. Chem.*, 2020, **59**, 16000–16009.
51 Y. Seki, H. Tabe and Y. Yamada, *J. Phys. Chem. C*, 2022, **126**, 5564–5574.
52 H. Tabe, S. Yorozu and Y. Yamada, *J. Phys. Chem. C*, 2022, **126**, 4365–4373.
53 Y. Shan, G. Zhang, W. Yin, H. Pang and Q. Xu, *Bull. Chem. Soc. Jpn.*, 2022, **95**, 230–260.
54 M. K. Nazeeruddin, R. Humphry-Baker, D. Berner, S. Rivier, L. Zuppiroli and M. Grätzel, *J. Am. Chem. Soc.*, 2003, **125**, 8790–8797.
55 K. Nakamoto, *Infrared and Raman Spectra of Inorganic and Coordination Compounds*, 4th edn, Wiley Interscience, 1986.
56 J. F. Moulder, J. K. Chastain and J. C. Roger, *Handbook of X-ray Photoelectron Spectroscopy*, 1995.
57 B. Bal, S. Ganguli and M. Bhattacharya, *J. Phys. Chem.*, 1984, **88**, 4575–4577.